ACS APPLIED MATERIALS & INTERFACES

Research Article

Cite This: ACS Appl. Mater. Interfaces 2018, 10, 43774−43784

www.acsami.org

Rubbing-Induced Site-Selective Growth of MoS_2 Device Patterns

Byunghoon Ryu, Da Li, Chisang Park, Hossein Rokni, Wei Lu, and Xiaogan Liang*

Department of Mechanical Engineering, University of Michigan, Ann Arbor, Michigan 48109, United States

Supporting Information

ABSTRACT: The superior electronic and mechanical properties of two-dimensional layered transition-metal dichalcogenides could be exploited to make a broad range of devices with attractive functionalities. However, the nanofabrication of such layered material-based devices still needs resist-based lithography and plasma etching processes for patterning layered materials into functional device features. Such patterning processes lead to unavoidable contaminations, to which the transport characteristics of atomically thin-layered materials are very sensitive. More seriously, such lithography-introduced contaminants cannot be safely eliminated by conventional semiconductor cleaning approaches. This challenge seriously retards the manufacturing of large arrays of layered material-based devices with consistent characteristics. Toward addressing this challenge, we introduce a rubbing-induced site-selective growth method capable of directly generating few-layer MoS_2 device patterns without the need of any additional patterning processes. This method consists of two critical steps: (i) a damage-free mechanical rubbing process for generating microscale triboelectric charge patterns on a dielectric surface and (ii) site-selective deposition of MoS_2 within rubbing-induced charge patterns. Our microscopy characterizations in combination with finite element analysis indicate that the field magnitude distribution within triboelectric charge patterns determines the morphologies of grown MoS_2 patterns. In addition, the MoS_2 line patterns produced by the presented method have been implemented for making arrays of working transistors and memristors. These devices exhibit a high yield and good uniformity in their electronic properties over large areas. The presented method could be further developed into a cost-efficient nanomanufacturing approach for producing functional device patterns based on various layered materials.

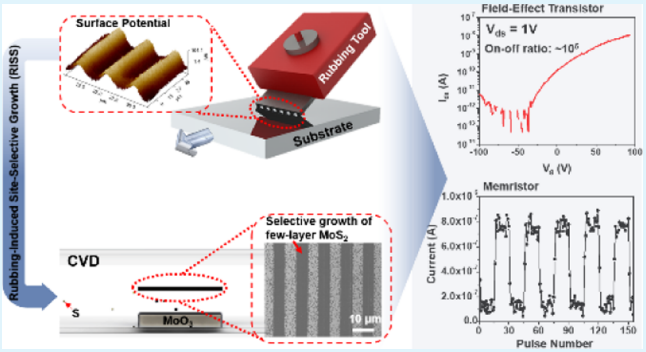

KEYWORDS: *nanofabrication, molybdenum disulfide, nanomanufacturing, chemical vapor deposition, field effect transistor, memristor*

INTRODUCTION

The interest in emerging two-dimensional (2D) layered transition-metal dichalcogenides (TMDCs, e.g., MoS_2, WSe_2, and WS_2) has soared because of their excellent electronic and mechanical properties, which could be exploited to fabricate a wide variety of functional devices with unprecedented and attractive functionalities.[1−6] In the fabrication of TMDC-based devices, the TMDC flakes are mechanically transferred (or printed) from a bulk ingot to the substrate, or the TMDC films are grown on the substrate using deposition methods such as chemical vapor deposition (CVD) and atomic layer deposition.[7−13] However, to manufacture commercially viable arrays of TMDC devices with consistent characteristics, the sizes and locations of TMDC device features must be well controlled in the fabrication. Therefore, additional resist-based lithography and plasma-based etching processes need to be performed to pattern as-deposited TMDC layers into functional device features. It is worthwhile to note that such device patterning processes inevitably introduce a broad range of contaminants that complicatedly modify and degrade the transport characteristics of electronic devices. The transfer characteristics of TMDC-based devices are especially sensitive to these contaminants because of their atomically thin structures.[14−18] More seriously, conventional semiconductor cleaning approaches (e.g., RCA and piranha methods) cannot safely eliminate such lithography-introduced contaminants without causing additional chemical/physical damages to TMDC patterns. This is because of the fact that atomically thin TMDC structures are very fragile in these cleaning reagents, and also because of the fact that most layered materials with 2D surfaces have a weak adhesion to dielectric substrates and are easily peeled off by the bubbling of gases during the cleaning processes.[19,20] Therefore, although deposition-lithography−etching-metallization method is being widely used in the industry for processing conventional semiconductor structures, it is still not suitable for producing 2D layered semiconductor devices.

To address such a general challenge in the patterning of emerging layered materials, it is highly desirable to develop site-selective growth techniques capable of directly generating

Received: August 31, 2018
Accepted: November 28, 2018
Published: November 28, 2018

DOI: 10.1021/acsami.8b15108
ACS Appl. Mater. Interfaces 2018, 10, 43774−43784

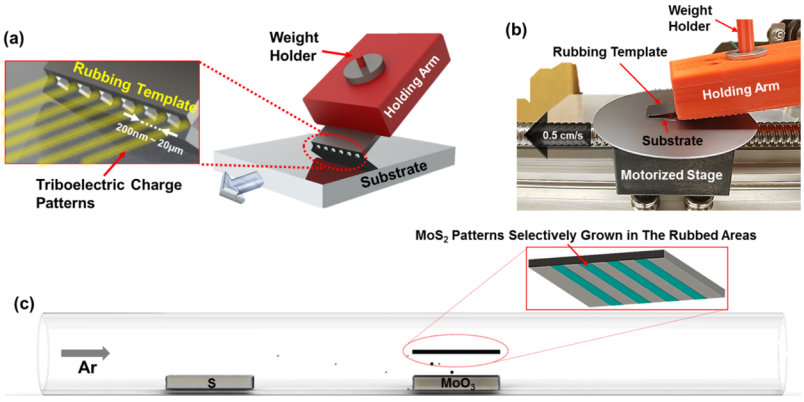

Figure 1. Setup of the RISS process: (a) schematic illustration of a rubbing tool for generating triboelectric charge patterns on a target substrate; (b) photography of a lab-made rubbing tool; (c) illustration of the site-selective CVD growth of few-layer MoS_2 patterns on a RISS-processed substrate.

TMDC and other layered material-based device patterns, without the need of (or with a minimal usage of) additional lithography and etching processes. Han et al. reported using patterned nucleation seeds to grow MoS_2 crystals at predetermined locations using CVD.[21] Sun et al. demonstrated the site-selective growth of MoS_2 structures within prepatterned topographical features.[22] More recently, Chen et al. demonstrated the selective growth of MoS_2 on a chemically treated substrate.[23] In these previously reported methods, some types of guiding features must be introduced onto the substrates for realizing site-selective growth. A potential concern is that these guiding features cannot be removed after the fabrication and might also lead to complicated effects on the device performance. Therefore, additional efforts are needed to explore the viability of a method capable of directly generating MoS_2 patterns without introducing any permanently existing features on the substrates.

In this article, we present a rubbing-induced site-selective growth (RISS) method capable of producing few-layer MoS_2 patterns without the need of additional patterning steps. Such a lithographic capability for generating MoS_2 device structures has not been reported yet. In a RISS process, a SiO_2 growing substrate is first rubbed by a motorized rubbing template bearing topographic structures, which generates surface charge patterns because of the triboelectric effect. Afterward, the rubbed SiO_2 substrate is loaded into a CVD tube, and few-layer MoS_2 patterns are selectively grown within the rubbed areas on the SiO_2 substrate. In this work, the fabrication of MoS_2 line/spacing patterns with different periods ranging from 200 nm to 20 μm has been specifically demonstrated. Kelvin probe force microscopy (KPFM) analysis in combination with finite element analysis (FEA) simulation shows that the RISS-produced MoS_2 patterns are well correlated to the triboelectric field distribution within rubbed surface areas. Furthermore, the RISS-produced MoS_2 line/spacing features have been utilized for making arrays of field-effect transistors (FETs) and lateral two-terminal memristors. These devices exhibit a high yield of ~76% and a good device-to-device consistency in their critical performance parameters. Specifically, the fabricated FETs exhibit reasonably high on−off ratios in the range of 10^3 to ~10^6 and an average field-effect mobility of 0.18 ± 0.17 $cm^2/(V\,s)$. The memristors made from RISS-produced MoS_2 channels exhibit a low threshold field magnitude (~10^4 V/cm) for initiating memristive switching courses, a high switching ratio of ~8, and a small relative standard deviation (~3%) in the set/reset currents measured from multiple memristors.

RESULTS AND DISCUSSION

Figure 1 illustrates our setup for demonstrating RISS. Specifically, Figure 1a schematically illustrates our lab-made tool for generating triboelectric charge patterns on a dielectric substrate through a rubbing process. In such a rubbing process, a rubbing-purposed template bearing topographic features is obliquely mounted on a holding arm. When a mass weight is added to the holding arm, the edge of the rubbing template is brought into contact with the substrate, and the contact force between the template and the substrate can be well controlled by adjusting the mass weight added to the holding arm. Carried by a motorized stage, the substrate moves in respect to the rubbing template, and the topographic features at the template edge gently rub the substrate. In case that the template and the substrate are made from materials with different triboelectricity coefficients, triboelectric charge is generated within the rubbed regions on the substrate. In principle, this rubbing tool could generate arbitrary triboelectric charge patterns through a combination of the design of the rubbing template features and the control of the stage motion. However, in this work, we specifically use the templates bearing line/spacing features (period: 200 nm to 20 μm; duty cycle: 50%) for experimentally demonstrating RISS and investigating its fundamental processing characteristics, as illustrated by the magnified inset view in Figure 1a. In addition, the line/spacing features can be generically exploited to make a broad range of densely arranged electronic devices, such as thin-film transistors (TFTs), memories, memristors, and multiplexing biosensors. Figure 1b shows a photograph of our lab-made rubbing tool. In this rubbing tool, the holding arm is made of polylactic acid plastic and fabricated by using a three-dimensional (3D) printer. A motorized stage controlled by an Arduino microcontroller is used for generating precisely controlled translational motion of the substrate in respect to the rubbing template. The moving speed of the stage is set to 0.5 cm/s during a rubbing process. After a rubbing process, the substrate with rubbing-induced triboelectric charge patterns is loaded into a CVD for performing selective growth of MoS_2 patterns, which is mediated by the electric field generated by the charge patterns, as illustrated in Figure 1c. RISS is a scalable nanofabrication process and could be used for manufacturing MoS_2 device patterns over large areas. More details about the RISS process are described in the Methods and Materials section. In addition, the supplementary video in the Supporting Information demonstrates a rubbing process driven by our rubbing tool.

DOI: 10.1021/acsami.8b15108
ACS Appl. Mater. Interfaces 2018, 10, 43774−43784

Figure 2 shows the KPFM characterization of the triboelectric charge pattern formed on a SiO_2 substrate. Specifically, Figure 2a,b displays the optical micrograph (OM) and tilted-view scanning electron micrograph (SEM) of a Si-based rubbing template bearing line/spacing features with a period of 20 μm, protrusive line width of 10 μm, depth of 5 μm, and duty cycle of 50%, respectively. This template is used for rubbing the substrate and generating triboelectric charge patterns. In our experiments, we found that the rubbing between Cu and SiO_2 surfaces results in very prominent triboelectric effect. This is because Cu and SiO_2 have completely opposite triboelectric polarities and stay quite far away from each other on the triboelectric series, as shown in Figure S1. In addition, Cu is chosen as the material for making rubbing templates and also because of its high compatibility with low-cost deposition processes, good mechanical and chemical stabilities, and large abundance. Therefore, the rubbing template is coated with 5 nm Cu by electron-beam evaporation, aiming to generate prominent and consistent triboelectric charge patterns on SiO_2 substrates. More details about the fabrication of the rubbing template are described in the Methods and Materials section. In such a rubbing test, the substrate is rubbed by the line/spacing template under a contact force of 100 mN (the corresponding contact gauge pressure is 443.5 MPa, which is estimated using the method described below). Figure 2c displays the topographic atomic force microscopy (AFM) image of the rubbed area on the SiO_2 substrate, which does not exhibit any rubbing-induced mechanical damage to the SiO_2 surface. Figure S2 in the Supporting Information shows that the root-mean-square (rms) values of surface roughness (R_q) measured from both rubbed and unrubbed areas on a SiO_2 surface do not exhibit a statistical difference. Figure S3 in the Supporting Information displays the X-ray photoelectron spectroscopy (XPS) (Figure S3a) and contact angle measurement (Figure S3b) results acquired from a SiO_2 surface before and after being rubbed by a Cu rod template (rubbing pressure ~500 MPa). Figure S3a shows that the XPS spectrum measured from the rubbed area does not exhibit a noticeable Cu peak. Figure S3b shows that the water contact angle on this SiO_2 surface does not noticeably change after the rubbing process. These results show that the rubbing process does not result in observable Cu contamination or modification of surface wettability. Figure 2d shows the KPFM image (i.e., surface potential image) of the same rubbed area on the substrate. This KPFM image clearly shows a grating-like pattern of electric potential, which is highly consistent with the line/spacing feature on the rubbing template and is reasonably attributed to the triboelectric charge induced by the rubbing between the Cu-coated line/spacing template and the SiO_2 substrate.[24] In this rubbing test, the resulted peak-to-valley amplitude of potential fluctuation on the SiO_2 substrate is measured to be ~100 mV, which is the typical condition for the

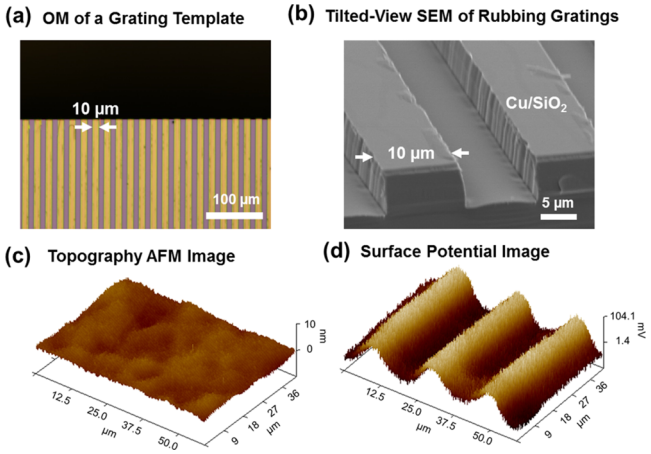

Figure 2. AFM and KPFM characterizations of a SiO_2 substrate area rubbed by a rubbing template: (a) OM and (b) tilted-view SEM of a 20 μm period Cu-coated Si rubbing template (protrusive linewidth: 10 μm, feature height: 5 μm); (c) topography AFM image of the SiO_2 surface area rubbed by the rubbing template under a contact pressure of 443.5 MPa, which does not show any visible rubbing-induced damage to the surface; (d) KPFM image (i.e., surface potential image) of the same surface area, which clearly exhibits a high-contrast grating-like potential profile, highly correlated to the features on the rubbing template.

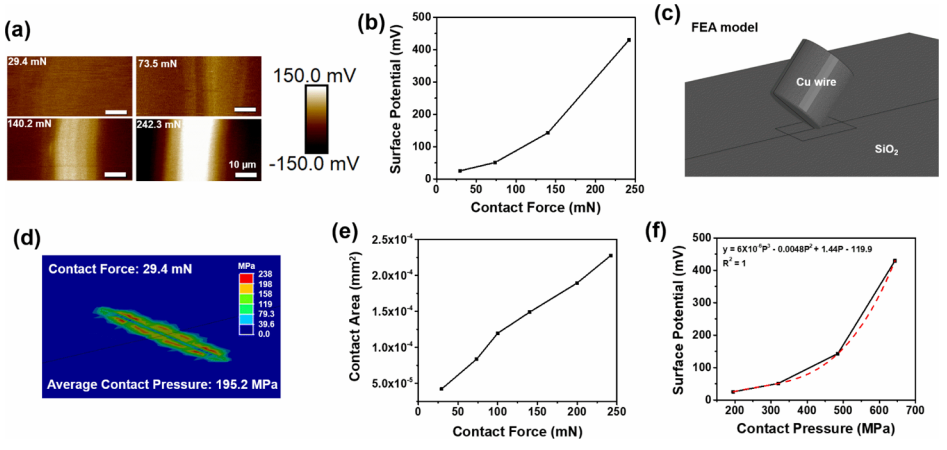

Figure 3. KPFM analysis in combination with FEA to investigate the functional relationship among surface potential (φ), contact force (F), and contact pressure (P): (a) KPFM images captured from SiO_2 surface areas, which were rubbed by a Cu rod template under different contact forces of 29.4, 73.5, 140.2, and 242.3 mN, respectively; (b) KPFM-measured surface potentials (φ) vs corresponding applied contact forces (F); (c) illustration of the FEA model for simulating the contact between the Cu rod template and the SiO_2 surface; (d) FEA-calculated distribution of the gauge pressure at the Cu/SiO_2 interface under a contact force of 29.4 mN; (e) FEA-calculated effective contact areas (A) plotted as a function of contact forces (F); (f) KPFM-measured surface potentials (φ) plotted as a function of corresponding FEA-calculated contact pressures (P), which can be fitted by an empirical polynomial function ($\varphi = 6 \times 10^{-6}P^3 - 0.0048P^2 + 1.44P - 119.9$), as denoted by the red line.

DOI: 10.1021/acsami.8b15108
ACS Appl. Mater. Interfaces 2018, 10, 43774−43784

subsequent site-selective CVD growth of MoS_2 patterns. We further investigated the effect of heat treatment on the surface potential induced by triboelectric effect. Figure S4 in the Supporting Information shows the KPFM surface potential images of a rubbed SiO_2 surface captured before and after heat treatment. Specifically, Figure S4a shows the photograph of a CVD furnace tube (filled with 150 sccm of Ar gas), in which a SiO_2 substrate rubbed by a Cu rod template is subjected to a heat treatment process at 800 °C for 3 min. Figure S4b shows the KPFM surface potential image of the SiO_2 surface before heat treatment. In Figure S4b, the white line denotes a potential profile, from which the peak value of surface potential is measured to be ~56.1 mV. Figure S4c displays the KPFM surface potential image of the same SiO_2 surface after heat treatment. Figure S4c shows that after heat treatment, the peak value of surface potential is measured to be ~15.6 mV, which is ~70% lower than that measured before heat treatment. Such a heat-induced reduction of surface potential is attributed to the thermally enhanced diffusion of charged carriers on the SiO_2 surface. Nevertheless, the rubbing-induced surface potential, even after heat treatment at a typical growth temperature (~800 °C), is still prominent and can serve as effective triboelectric charge patterns for inducing selective MoS_2 growth.

Given the template/substrate materials that rub to each other, the resulted triboelectric charge density, field magnitude, or surface potential on the dielectric substrate is expected to depend on the applied contact force (or gauge pressure) between the template and the substrate.[25,26] To obtain a precise control of the RISS processes, we investigated the functional relationship among surface potential (φ), contact force (F), and contact pressure (P) through KPFM analysis in combination with FEA modeling. Specifically, in this study we used a cylindrical Cu rod (diameter: 0.5 mm) instead of the line/spacing structures as the rubbing template. This is because the mechanical deformation of a cylindrical rod template can be easily simulated for precisely quantifying the effective contact area (A) as well as gauge pressure (P) between the template and the substrate. We assume that the φ–P relationship acquired from this cylindrical Cu rod template is also applicable to other Cu-coated templates. Figure 3a displays a series of KPFM images captured from the SiO_2 surface areas rubbed by the same Cu rod exerted with different contact forces (i.e., F = 29.4, 73.5, 140.2 and 242.3 mN). The resulted surface potential (φ) values are extracted from these KPFM images and plotted as a function of contact forces in Figure 3b. Because during the rubbing experiment, it was extremely hard to directly measure the effective contact area (A) between the rod template and the substrate, we established a FEA model and used a commercial FEA software package (ABAQUS) to evaluate the effective contact area values under different contact forces. Figure 3c illustrates the FEA model, in which the cylindrical Cu rod template (diameter: 0.5 mm) is inclined by 45° and its edge is in contact with the underlying SiO_2 surface. This model is consistent with the corresponding experimental setup. More details about this FEA model are described in the Methods and Materials section as well as Figure S5 in the Supporting Information. Figure 3d shows a representative FEA result of the gauge pressure distribution at the template/substrate interface under a contact force of 29.4 mN. The corresponding contact area (A) and average contact pressure (P) between the template and the substrate can be extracted from such a FEA result. Figure 3e plots the FEA-calculated contact areas (A) with respect to the corresponding contact forces (F) applied in the experiment, from which the corresponding average contact pressures (P) can be also calculated. Figure 3f plots KPFM-measured surface potential (φ) values versus FEA-calculated contact pressures (P). Such φ–P data can be tentatively fitted by an empirical polynomial function ($\varphi = 6 \times 10^{-6}P^3 - 0.0048P^2 + 1.44P - 119.9$), as denoted by the red dashed line in Figure 3f. This φ–P curve could be used for determining the contact gauge pressure required for generating the triboelectric charge pattern with a given surface potential and also determining if such a rubbing condition induces any damage to the substrate. For example, in this work we identified that the triboelectric charge patterns with a surface potential of 100 mV can result in effective site-selective growth of MoS_2 patterns. On the basis of the φ–P curve in Figure 3f, the gauge pressure required for performing the rubbing process to generate such charge patterns is estimated to be 443.5 MPa. This pressure value is about a quarter of magnitude lower than the compressive strength of SiO_2 and does not cause serious damage to the SiO_2 substrate, as indicated by the AFM result in Figure 2c. The contact pressure exerted during a rubbing process cannot exceed the compressive strength (σ_c) of the substrate (e.g., for a SiO_2 substrate, σ_c is the range of 1.1–1.6 GPa). Given such a maximum possible contact pressure value, the corresponding maximum surface potential can be estimated by using our empirical polynomial function discussed above (i.e., $\varphi = 6 \times 10^{-6}P^3 - 0.0048P^2 + 1.44P - 119.9$). Using this empirical function, the maximum surface potential value is estimated to be around 3.6 V.

Figure 4 displays the SEM images of a series of RISS-produced few-layer MoS_2 line/spacing patterns with different periods/

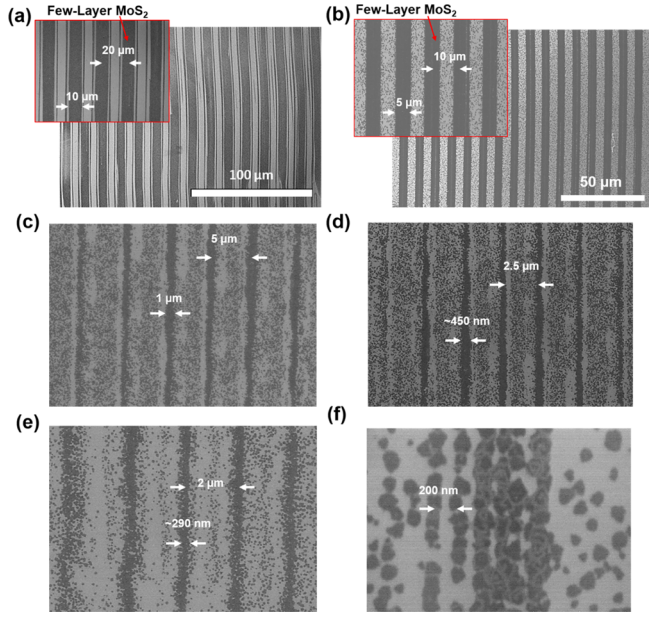

Figure 4. SEM images of representative RISS-produced few-layer MoS_2 lines with different periods/linewidths of (a) 20 μm/10 μm, (b) 10 μm/5 μm, (c) 5 μm/1 μm, (d) 2.5 μm/~450 nm, (e) 2 μm/~290 nm, and (f) ~250 nm/not applicable.

effective linewidths ((a) 20 μm/10 μm, (b) 10 μm/5 μm, (c) 5 μm/1 μm, (d) 2.5 μm/~450 nm, (e) 2 μm/~290 nm, and (f) ~250 nm/not applicable). Here, the effective linewidth of a RISS-produced MoS_2 line is defined as the average linewidth of the region, in which MoS_2 grains are connected to each other to form a continuous channel line, not including the dispersed

DOI: 10.1021/acsami.8b15108
ACS Appl. Mater. Interfaces 2018, 10, 43774–43784

MoS_2 grains around this continuous line. For all MoS_2 line/spacing patterns, their periods are consistent with the periods of the corresponding rubbing template features. This indicates that in a RISS process, the rubbing by the Cu-coated template can induce site-selective growth of MoS_2 features on the rubbed SiO_2 substrate. The grain sizes of isolated single crystal MoS_2 flakes grown in the marginal areas of RISS-produced MoS_2 lines are in the range of 200−300 nm, as indicated by the SEM images in Figure S6b. To further evaluate the grain sizes in the central areas of RISS-produced few-layer MoS_2 lines, we annealed the MoS_2 lines under air conditions at 150 °C for 10 min and subsequently captured the AFM phase images of these annealed MoS_2 features. Currently, phase-mode AFM imaging in combination with annealing has become a valid tool for visualizing the grain boundaries within a continuous polycrystalline MoS_2 film.[27−29] Especially, through a mild sample oxidation course in the air, the grain boundaries within a MoS_2 film can be recognized by composition-sensitive microscopies (e.g., phase-mode AFM and back-scattered SEM) because of their altered contrasts.[30] The AFM phase image in Figure S6c indicates that the central area of a RISS-produced MoS_2 line indeed exhibits the smaller grain sizes (95−220 nm) in comparison with its marginal areas. Such relatively smaller MoS_2 grains are attributed to the abundant nucleation sites within the rubbed SiO_2 areas, which limit the average range of lateral epitaxial growth of MoS_2 grains.[23,31] The average thickness of RISS-produced MoS_2 lines is 3.55 ± 0.67 nm, which is measured from the MoS_2 lines distributed over a ∼0.25 cm^2 area by using AFM. The representative AFM image and the extracted statistical thickness data are presented in Figure S7. Figure S8 in the Supporting Information further shows Raman characterization results of few-layer MoS_2 lines produced by a RISS process. Specifically, Figure S8a displays the optical micrograph of RISS-produced MoS_2 lines with a period/linewidth of 10 μm/5 μm. Figure S8b displays the Raman spectrum acquired from the central region of a MoS_2 line (excitation laser wavelength: 532 nm), which exhibits two Raman scattering peaks associated with two characteristic phonon modes of MoS_2 layers (i.e., E^1_{2g} and A_{1g} peaks appearing at ∼383 and ∼407 cm^{-1}, respectively). On the basis of the spacing between these two peaks (∼24 cm^{-1}) in combination with their positions, the thicknesses of RISS-produced MoS_2 lines are estimated to be in the range of 4−5 layers,[32,33] which is in good agreement with our AFM-measured thickness data shown in Figure S7. Figure S8c,d displays the Raman mapping images of MoS_2 lines based on E^1_{2g} and A_{1g} modes, respectively. These two images show that strong E^1_{2g} and A_{1g} scattering signals only appear within the rubbed areas. This result further indicates the selective growth capability of RISS. The same Raman spectrum is also plotted with the full Raman shift range in Figure S9. This spectrum does not exhibit prominent peaks at 149, 195, 280, 344, 650, and 820 cm^{-1}, which are characteristic features associated with the stretching and bending vibration modes of Mo═O and O−Mo−O bonds.[34] The lack of such modes in combination with the prominent E^1_{2g} and A_{1g} features strongly indicates that most precursor molecules have been well converted to MoS_2 layers in our CVD growth.[34]

In this prototype demonstration work, the processing area of our RISS system is at the mm^2 scale, which is mainly limited by the size of the rubbing templates but could be further increased by using larger templates and optimizing the template/substrate contact. Currently, our lab-made CVD system cannot enable the precise control of the number of MoS_2 layers. However, control of the number of MoS_2 layers during a CVD process is a generic challenge about the CVD process and is not directly associated with our RISS method. As demonstrated above, our current RISS process can produce few-layer MoS_2 lines with an average thickness of 3.55 ± 0.67 nm. Such few-layer MoS_2 structures are already useful for a series of device applications, such as TFT, photodetectors, memories, memristors, and biosensors.[2,6,35]

To evaluate the morphological characteristics of RISS-produced MoS_2 lines, we introduce a specific cover ratio parameter that is defined as the percentage of the local area covered by as-grown MoS_2 layers (or grains). Figure 4 shows that for a RISS-produced MoS_2 line, the cover ratio of its central area is high and usually in the range of 80−100%, whereas its edge regions exhibit a gradual variation of the cover ratio. For the MoS_2 lines produced by the rubbing features with linewidths larger than 2 μm (e.g., the samples shown in Figure 4a,b), such a gradual variation of the cover ratio at the feature edges does not significantly affect their effective linewidths, and the effective linewidths of these relatively wide MoS_2 lines are mainly determined by the linewidths of the rubbing template features. However, for the MoS_2 lines produced by the rubbing features with relatively smaller linewidths (e.g., those shown in Figure 4c−f), such a gradual variation of cover ratio at feature edges results in significantly smaller effective linewidths in comparison with the corresponding linewidths of the rubbing features. As shown in Figure 4f, the MoS_2 lines produced by a rubbing template with a feature period of 200 nm and a linewidth of 100 nm are not even continuous because of the overly dispersive variation of MoS_2 cover ratio at the edges.

Such a gradual variation of MoS_2 cover ratio at the edges of RISS-produced features is attributed to the net effect of (1) the field magnitude distribution within rubbing-induced triboelectric charge patterns and (2) the diffusion of nucleated MoS_2 domains from triboelectric charge pattern areas.[36] To quantitatively correlate the spatial distribution of rubbing-induced triboelectric field and the distribution of resulted MoS_2 cover ratio, we used a FEA model to simulate the electric field associated with the triboelectric charge on a SiO_2 surface and compared this simulated field distribution to the MoS_2 cover ratio profile measured from the SEM image of the corresponding MoS_2 sample. Specifically, a MATLAB-based imaging tool was used for processing SEM images and measuring MoS_2 cover ratio profiles, and a COMSOL software package was used for FEA simulation. The details related to image processing and FEA are described in the Supporting Information and Methods and Materials section, respectively. Figure S10 in the Supporting Information shows the comparison between the electric field distribution measured by KPFM and that simulated by FEA. Specifically, Figure S10a shows the KPFM image of a SiO_2 surface rubbed by a line/spacing template with a period/linewidth of 20 μm/10 μm. This KPFM image displays a grating-like surface potential distribution with a period of 20 μm. A surface potential profile is captured from the location denoted by a dashed line and plotted as the solid curve, as shown in Figure S10b. In Figure S10b, the surface potential profile simulated by FEA (dashed curve) is also plotted and compared to that obtained by KPFM. On the basis of these two surface potential profiles, the profiles of field magnitude distribution obtained from KPFM and FEA are calculated and plotted together in Figure S10c. Figure S10b,c indicates that the electric field distribution measured by KPFM is in good agreement with that obtained from FEA simulation. This comparison shows that FEA can serve as a valid tool for simulating and analyzing the

DOI: 10.1021/acsami.8b15108
ACS Appl. Mater. Interfaces 2018, 10, 43774−43784

electric field involved in a RISS process. Figure 5 displays a representative analysis for the MoS_2 lines shown in Figure 4d,

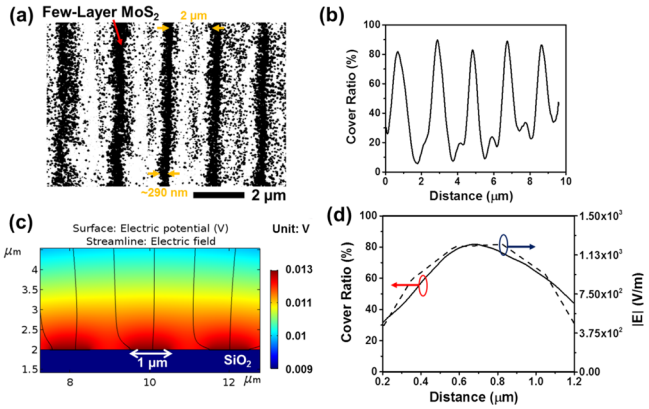

Figure 5. Cover ratio analysis for relatively narrow RISS-produced MoS_2 lines (period/linewidth: 2 μm/~290 nm): (a) binary SEM image of the MoS_2 lines; (b) MoS_2 cover ratio profile across the MoS_2 lines, which are extracted from the binary SEM image; (c) FEA-simulated electric field associated with the corresponding rubbing-induced triboelectric charge pattern (i.e., line/spacing charge pattern with period/linewidth of 2 μm/1 μm); (d) FEA-simulated triboelectric field magnitude profile (dashed line) and SEM-measured MoS_2 cover ratio profile (solid line) around a triboelectric charge line area.

which were produced by using a rubbing template with a period of 2 μm and a linewidth of 1 μm. Figure 5a shows the binary SEM image processed from Figure 4d, from which the MoS_2 cover ratio profile across the MoS_2 lines is extracted and plotted in Figure 5b. Figure S11 shows the image processing process to calculate the cover ratio of RISS-produced MoS_2 lines. Specifically, the original SEM image of MoS_2 lines is processed into a binary image using Otsu's algorithm and the local pixels covered by MoS_2 (i.e., the dark pixels shown in the binary SEM image) are counted.[37] The detailed process for extracting the cover ratio profile is described in the Supporting Information. Figure 5b shows that the MoS_2 cover ratio distribution across these relatively narrow MoS_2 line features has a sine-like profile with peak values in the range of 80−92% (i.e., the cover ratios measured from the central regions of the MoS_2 lines) and valley values in the range of 6−30% (i.e., the cover ratios measured from the central regions of the unrubbed areas). Figure 5c shows the FEA-simulated electric field from the triboelectric charge regions on a SiO_2 surface. In this FEA simulation, we assume a uniform charge density within the rubbed areas, which are 2 μm period and 1 μm wide lines. The value of the charge density is set so that the potential at the central areas of the lines is 100 mV, which is consistent with the potential measured by KPFM, as shown in Figure 2d. From Figure 5c, the field magnitude profile around a single charge line is extracted and plotted as a dashed line in Figure 5d. For comparison, the cover ratio profile measured around a representative MoS_2 line in Figure 5a is also plotted as a solid line in Figure 5d. Figure 5d indicates that the spatial distribution profiles of field magnitude and MoS_2 cover ratio around a triboelectric charge line area have very similar shapes and exhibit a strong correlation to each other. Quantitatively, the field magnitude in the middle of a rubbed line is ~1.2×10^3 V/m that leads to a local RISS-produced MoS_2 cover ratio of ~80%, whereas the field magnitude at the edges of the rubbed line is ~450 V/m that leads to a relatively low cover ratio of 30−45%.

Figure 6 further shows the analysis results for the MoS_2 lines produced by using a rubbing template with a period of 10 μm

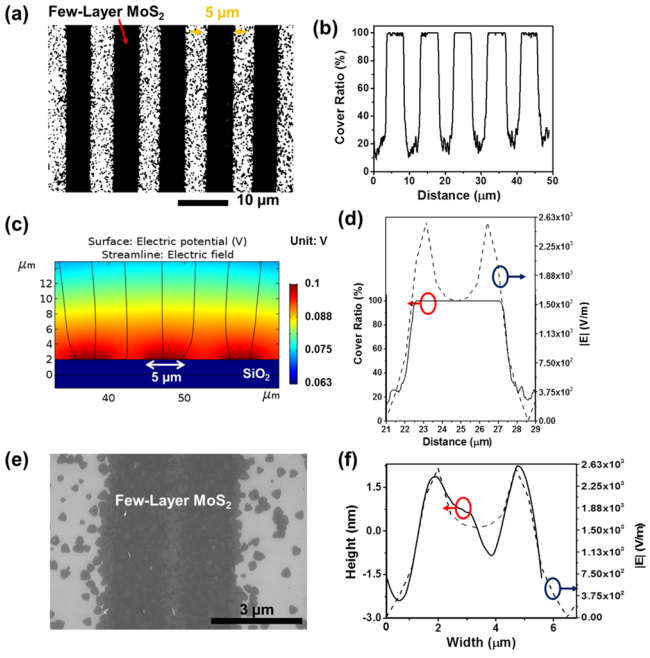

Figure 6. Cover ratio and thickness analysis for relatively wide RISS-produced MoS_2 lines (period/linewidth: 10 μm/5 μm): (a) binary SEM image of the MoS_2 lines; (b) MoS_2 cover ratio profile across the MoS_2 lines, which are extracted from the binary SEM image; (c) FEA-simulated electric field associated with the corresponding rubbing-induced triboelectric charge pattern (i.e., line/spacing charge pattern with period/linewidth of 10 μm/5 μm); (d) FEA-simulated triboelectric field magnitude profile (dashed line) and SEM-measured MoS_2 cover ratio profile (solid line) around a triboelectric charge line area; (e) zoomed SEM image of a 5 μm wide RISS-produced MoS_2 line; (f) AFM-measured height profile (solid line) of the MoS_2 line and FEA-simulated triboelectric field magnitude profile (dashed line).

and a linewidth of 5 μm (i.e., the sample shown in Figure 4b). Figure 6a,b shows the binary SEM image and the extracted MoS_2 cover ratio profile across multiple lines, respectively. These two figures show that for such relatively wide MoS_2 lines (typically those produced by the rubbing features with linewidths larger than 2 μm), the MoS_2 cover ratio is ~100% for the almost entire rubbed area. Such a high contrast of MoS_2 patterns is expected as a result of the high contrast distribution of field magnitude within the rubbed line areas. Figure 6c displays the FEA-calculated electric field associated with the triboelectric charge within the 5 μm wide rubbed line areas on a SiO_2 surface. Other simulation parameters are the same as those for the one shown in Figure 5c. From Figure 6c, the field magnitude profile across a single 5 μm wide charge line is extracted and plotted as a dashed line in Figure 6d. This field distribution profile is compared with the cover ratio profile measured around a MoS_2 line shown in Figure 6a (i.e., the solid line in Figure 6d). Different from the field magnitude profile around a 1 μm wide rubbed SiO_2 line (see Figure 5c), the field distribution around a 5 μm wide rubbed line exhibits two peaks at the line edges. The presence of these two peaks makes the electric field magnitude over the entire rubbed area higher than 1.5×10^3 V/m, which results in a high cover ratio of ~100% for almost the whole rubbed area. Figure 6d also shows that triboelectric field magnitude and RISS-produced MoS_2 cover ratio exhibit a strong correlation, which is

DOI: 10.1021/acsami.8b15108
ACS Appl. Mater. Interfaces 2018, 10, 43774−43784

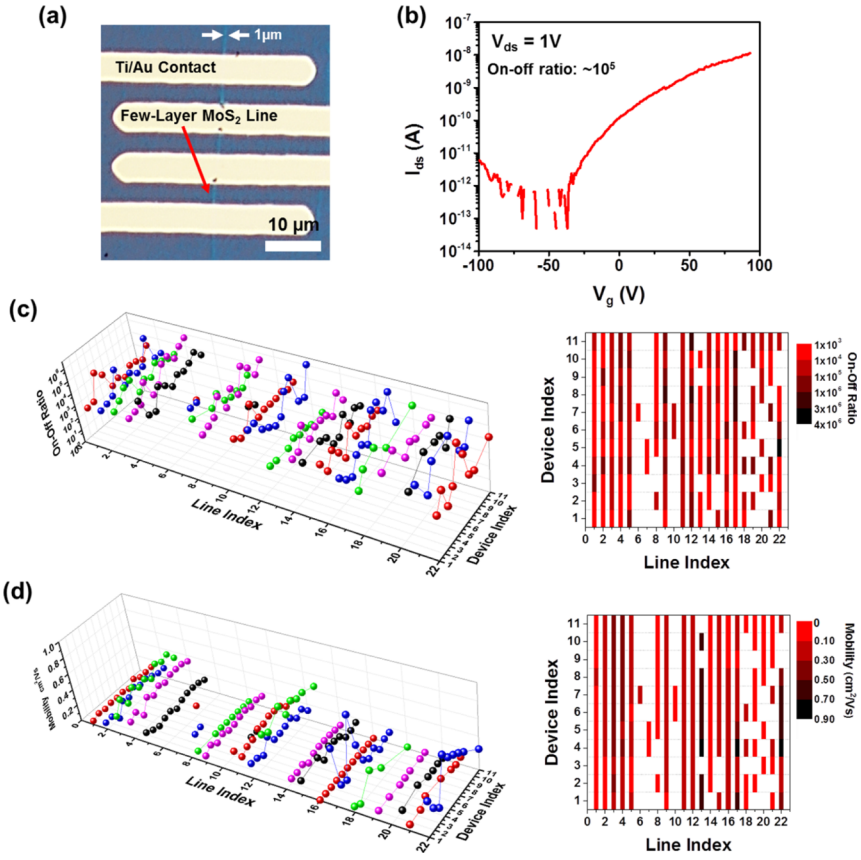

Figure 7. Demonstration of an array of working FETs fabricated on RISS-produced few-layer MoS_2 lines: (a) optical micrograph of three representative back-gated MoS_2 FETs fabricated on a MoS_2 line (FET channel length: 5 μm, width: ~1 μm); (b) transfer characteristic (or $I_{ds}-V_g$) curve of a representative MoS_2 FET; (c) 3D (left) and 2D top-view (right) plots of the on−off ratio data measured from 184 working FETs on the same substrate as the function of line and device indexes; (d) 3D (left) and 2D top-view (right) plots of the field-effect mobility data measured from 184 working FETs as the function of line and device indexes.

consistent with the field/cover-ratio correlation observed in Figure 5d for the relatively narrower MoS_2 lines. This implies that in a RISS process, the local triboelectric field magnitude is a key factor affecting the nucleation of precursor molecules and therefore the local MoS_2 cover ratio.

It is further noted that although a local triboelectric field magnitude higher than 1.5×10^3 V/m makes the local MoS_2 cover ratio saturate to ~100%, different field magnitudes above this saturating value still result in different local MoS_2 thicknesses. Specifically, Figure 6e shows a zoomed SEM image of a 5 μm wide RISS-produced MoS_2 line. In this SEM image, the darkness distribution across the MoS_2 line implies that the edge areas of the MoS_2 line are relatively thicker than its central area. This has been further verified by our AFM characterization. Figure 6f plots an AFM height profile curve (solid line) acquired across the MoS_2 line as well as a FEA-calculated field magnitude profile. The AFM profile curve specifically indicates that from the center of the MoS_2 line to its edges, the MoS_2 thickness varies from 1.5 nm (~two layers) to 3 nm (~four layers). Such a variation profile for MoS_2 thickness has a very similar shape as that of the field magnitude profile. This further supports our conclusion that in a RISS process, the local triboelectric field magnitude is the key factor affecting the nucleation rate of precursor molecules. Here, it should be also noted that, as shown in Figure 6a, the MoS_2 cover ratio measured from the unrubbed areas between continuous MoS_2 lines is ~20%, although the triboelectric field magnitude in such unrubbed areas is estimated to be negligible. Therefore, the MoS_2 grains observed in the unrubbed areas are mainly attributed to the lateral diffusion of the MoS_2 grains from the rubbed areas.

To evaluate the large-area uniformity of RISS-produced few-layer MoS_2 structures in their electronic properties, we fabricated FET arrays based on RISS-produced MoS_2 lines. To make such a FET array, 22 MoS_2 lines with an effective linewidth of ~1 μm are produced on a p^+-type Si substrate coated with 300 nm thick thermally grown SiO_2 using RISS. These MoS_2 lines have a large interline spacing of ~200 μm to provide footprint areas for Ti/Au contacts. Using our current mask set, 11 FETs with a channel length of 5 μm are fabricated on a single MoS_2 line. Therefore, an as-fabricated FET array consists of totally 242 FETs. The p^+-type Si substrate serves as the common back gate for these FETs. Other details about the FET fabrication are described in the Methods and Materials section. Figure 7a shows the optical micrograph of three representative FETs fabricated on a 1 μm wide MoS_2 line. The SEM image of one of these 1 μm wide MoS_2 FETs and the Raman spectrum measured from this FET channel are displayed in Figure S12a,b, respectively, in the Supporting Information. Figure 7b plots the transfer characteristic curve (i.e., drain−source current (I_{ds}) versus gate voltage (V_g) curve) measured from a representative back-gated MoS_2 FET. This FET exhibits a typical n-type transport behavior and its on−off ratio is ~10^5. The transfer characteristics measured from all other working

DOI: 10.1021/acsami.8b15108
ACS Appl. Mater. Interfaces 2018, 10, 43774−43784

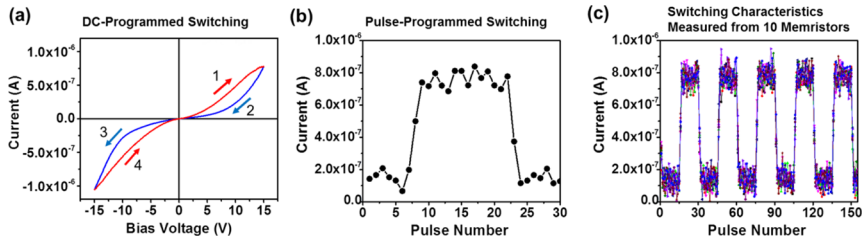

Figure 8. Demonstration of working memristors fabricated on RISS-produced few-layer MoS_2 lines: (a) dc-programmed switching characteristic curve (or hysteretic $I-V$ curve) measured from a representative MoS_2 memristor; (b) pulse-programmed switching characteristic curve measured from the same memristor (set process: 10 −30 V, 5 μs pulse; reset process: 10 +30 V, 5 μs pulses); and (c) pulse-programmed switching characteristic curves measured from 10 different memristors, which are plotted together to demonstrate a high device-to-device consistency in their switching characteristics.

FETs in the same array are listed in Figure S13 in the Supporting Information. The FETs shown in Figures 7b and S13 exhibit relatively low mobility and ON current values, which are attributed to the relatively narrow MoS_2 channel width (~1 μm). Figure S14a shows the optical micrograph of a set of FETs made from a 15 μm wide RISS-produced MoS_2 line (for all FETs, the channel length is still 5 μm), and Figure S14b displays the transfer characteristic curve of a representative FET. The ON current of such a relatively wider FET measured under a given condition is about two orders of magnitude higher than that of a 1 μm wide FET. The mobility values of such wider FETs are extracted to be higher than 1 cm^2/V s, and they are comparable with the mobility values of recently reported FETs made from CVD-grown MoS_2 films.[38−40] In the future, the mobility and ON current values of RISS-produced MoS_2 FETs are anticipated to be further improved through optimization of CVD conditions. Totally, 184 out of 242 as-fabricated FETs are properly working devices, and the fabrication yield is ~76%. This yield could be further improved through optimization of RISS and device fabrication processes. Figure 7c displays the on−off ratio data measured from these 184 FETs, which are plotted as the function of their line and device indexes. In Figure 7c, the left inset is the 3D plot, and the right inset is the 2D top-view plot that provides a clear view for the location distribution of working FETs in the array. On−off ratios measured from these FETs are in the range of 10^3 to ~3×10^6, which are reasonably high for most switching device applications. Figure 7d shows the 3D (left) and 2D (right) plots of the field-effect mobility data extracted from the transfer characteristics of the FETs. Specifically, the field-effect mobility of a FET is extracted by using eq 1, where ε_0 is the vacuum permittivity, $\varepsilon_r \approx 3.9$ is the relative permittivity of the SiO_2 dielectric layer, C_{ox} is the gate capacitance, and W/L is the width/length ratio of the MoS_2 FET channel.

$$\mu = \frac{1}{C_{ox}\frac{W}{L}V_{ds}}\left(\frac{dI_{ds}}{dV_g}\right) \qquad C_{ox} = \frac{\varepsilon_0\varepsilon_r}{d} \tag{1}$$

Figure 7d shows that the mobility values of the FETs range from 0.1 to 1 $cm^2/(V\ s)$ (mean value: 0.18 ± 0.17 cm^2/V s). Such relatively low mobility values are attributed to the relatively small average grain size within the MoS_2 channel lines.[23,31] During a site-selective growth process, the nucleation sites are highly localized and concentrated within the target growth areas. This results in very limited free space for a MoS_2 grain to grow before the local MoS_2 cover ratio reaches to 100%.[23,31] In addition, the relatively high contact resistance between MoS_2 channels and Ti/Au contacts could also affect the mobility value extracted using eq 1. Figure S15 in the Supporting Information shows the transfer length method (TLM) analysis of a set of four RISS-produced MoS_2 FETs with various channel lengths of 5, 10, 15, and 20 μm and the same channel width of 1 μm. From this analysis, the contact resistances under bias conditions of V_{DS} = 1 V, V_{GS} = 100 V and V_{DS} = 1 V, V_{GS} = 0 V are extracted to be 146 and 1520 kΩ mm, respectively, which are relatively higher than previously reported contact resistances for MoS_2/metal junctions.[39,41] Such relatively high contact resistances are temporarily attributed to the defects in RISS-produced MoS_2 layers, which could result in high Schottky barriers at MoS_2/metal interfaces. Our results imply that such Schottky barriers are highly dependent on the gate voltage. Future research effort will be performed to reduce such defects and improve the MoS_2/metal contact characteristics. Here, it is also noted that as shown in Figure 7c,d, the on−off ratio and mobility data measured from the FETs on the same MoS_2 line (i.e., the FETs with the same line index) exhibit a relatively smaller variance in comparison with those measured from the FETs on the different MoS_2 lines. Such a relatively large variance in the FET performance among lines is attributed to the variances in morphological parameters among RISS-produced MoS_2 lines, which could be further reduced by optimizing the large-area distribution of rubbing stress during the RISS processes.

Although the relatively small crystalline MoS_2 grains in RISS-produced MoS_2 lines result in relatively low field-effect mobility and are not very suitable for high-speed FET applications, they can form a 2D channel rich in movable defects (e.g., sulfur vacancies, molybdenum vacancies, antisites, and impurities) and potentially enable a niche application of RISS-produced MoS_2 structures in memristive electronics.[42] Although in a polycrystalline MoS_2 channel the long-distance migration of movable defects could be blocked by grain boundaries, the local migration of such defects around MoS_2/metal interfaces is still expected to result in an effective modulation of the Schottky barriers at MoS_2/metal interfaces and induces memristive switching processes.[43] To preliminarily demonstrate such a potential application, we fabricated and characterized memristor arrays based on RISS-produced MoS_2 lines, which have the same device structure as the FET array shown in Figure 7. Figure 8 shows the switching characteristics measured from such memristors. Specifically, Figure 8a shows the direct current (dc)-programmed switching characteristic curve (i.e., hysteretic $I-V$ curve) measured from a representative MoS_2 memristor, which exhibits a prominent memristive switching behavior. Additionally, such MoS_2 memristors exhibit a low threshold field magnitude for initiating memristive switching (~10^4 V/cm), which is about two orders of magnitude lower than that of the

DOI: 10.1021/acsami.8b15108
ACS Appl. Mater. Interfaces 2018, 10, 43774−43784

conventional memristors based on transition-metal oxides.[42,44] Figure 8b plots the pulse-programmed switching characteristic curve (i.e., current under a fixed voltage of 1 V versus number of applied pulses) measured from the same memristor (set process: 10 −30 V, 5 μs pulse; reset process: 10 +30 V, 5 μs pulses). During such a pulse-programmed switching cycle, the memristor current (measured under 1 V bias) gradually varies from ∼100 nA to ∼800 nA, indicating a switching ratio of ∼8. Such prominent memristive switching characteristics observed in our MoS_2 memristors are attributed to the high concentration of movable defects in RISS-produced MoS_2 channel lines that can dynamically modify the Schottky barriers at the MoS_2/contact interfaces and therefore modulate the conductance states of the memristors.[43] To analyze if rubbing-induced surface charge on SiO_2 surface could contribute to the observed memristive switching behavior, we transferred a RISS-produced MoS_2 line onto a pristine SiO_2/Si substrate without rubbing-induced charge. Figure S17a in the Supporting Information shows the optical micrograph of the two-terminal resistor made from this transferred MoS_2 line. Figure S17b displays the pulse-programmed switching characteristic curve measured from this resistor (measurement condition: set process: 10 −30 V, 500 ns pulses; reset process: 10 +30 V, 500 ns pulses). The switching ratio (i.e., ratio between the highest and lowest conductances during a switching cycle) of this device is measured to be ∼9, which is comparable to that measured from the MoS_2 devices on rubbed substrates. Such a result indicates that even on a pristine SiO_2/Si substrate without rubbing-induced charge, the resistor made from a RISS-produced MoS_2 line still exhibits a prominent memristive switching behavior and can serve as a memristor. This result also strongly implies that the observed memristive behavior of RISS-produced MoS_2 features is mainly attributed to the movable defects in the MoS_2 features. The future research will seek to identify the specific types of such defects. Figure 8c plots the pulse-programmed switching characteristic curves measured from ten memristors in the same array. These curves are also individually plotted in Figure S16 in the Supporting Information. These ten MoS_2 memristors exhibit a high device-to-device consistency in their memristive switching characteristics (the relative standard deviation in their set/reset currents is ∼3%) and could be further exploited for constructing neural network devices for neuromorphic computing applications. This result also indicates that RISS-produced MoS_2 channel lines exhibit a high uniformity in their concentrations of movable vacancies.

CONCLUSION

We developed and systematically studied a RISS method, which can enable scalable fabrication of few-layer MoS_2 device patterns without the need of additional patterning processes. In a RISS process, triboelectric charge patterns are generated on a target dielectric substrate surface by a template-based rubbing process and serves as highly preferential nucleation sites for the CVD growth of MoS_2 structures. Using RISS, we have specifically demonstrated the fabrication of MoS_2 line/spacing patterns with various periods and linewidths. Our microscopy characterization in combination with FEA simulation implied that the morphologies of RISS-produced MoS_2 patterns are strongly correlated with the field magnitude distribution within rubbing-generated triboelectric charge patterns. Finally, RISS-produced MoS_2 lines were used for making arrays of FETs and memristors, in which the yield of working devices was evaluated to be ∼76%, and both types of the devices exhibited a good device-to-device consistency. Specifically, the MoS_2 FETs showed reasonably high on−off ratios in the range of 10^3 to 3×10^6 and exhibited an average field-effect mobility of 0.18 ± 0.17 $cm^2/(V\ s)$. For the MoS_2 memristors, a large switching ratio of ∼8 and a low threshold field magnitude (∼10^4 V/cm) for initiating memristive switching are demonstrated. The presented RISS method could be further developed into a cost-efficient scalable nanomanufacturing technique capable of producing commercially viable device patterns based on various layered materials.

METHODS AND MATERIALS

Fabrication of a Rubbing Template. First, a photoresist (SPR 220) layer is spin-coated on a Si substrate. After a baking process at 115 °C for 5 min, the photoresist-coated Si substrate is aligned with a photomask bearing line/spacing patterns and exposed to UV light by using an aligner (MA6/BA6 mask aligner). After the development process, the Si substrate is etched in a plasma etcher (LAM9400) (etching condition: radio frequency power of 600 W, HBr flowrate of 100 sccm, He flowrate of 100 sccm). For all line/spacing patterns, the etching depth is 5 μm.

CVD Process. In a CVD process, 10 mg of molybdenum trioxide (MoO_3, 99.97%, Sigma-Aldrich) and 300 mg of sulfur (S, 99.5%, Sigma-Aldrich) are placed at the center and upstream locations of a 1″-diam quartz tube, respectively. The SiO_2 or other dielectric substrates bearing rubbing-induced triboelectric charge patterns serves as the target substrates. These substrates are placed face-down above the MoO_3 source. Ar (99.999%, Cryogenic Gases) is used as the carrier gas, and the gas flow rate is set to 150 sccm during the synthesis course. The temperature of the central area of the furnace chamber rises to 800 °C and maintains the same for 5 min during the MoS_2 synthesis. Afterward, the furnace is cooled to the room temperature, and the substrates bearing RISS-produced MoS_2 patterns are taken out from the quartz tube.

FEA for Investigating the Relationship Among Surface Potential (φ), Contact Force (F), and Average Contact Pressure (P). A commercial FEA software package (ABAQUS) is used for modeling the contact between the Cu rod template (diameter: 0.5 mm) and the SiO_2 substrate surface. The Young's modulus/Poisson's ratio of the Cu rod template and the SiO_2 substrate are set to 117 GPa/0.33 and 70 GPa/0.15, respectively. Figure S5 displays the FEA model and the mesh setup. In this model, the surface-to-surface contact between the Cu rod and the SiO_2 surface is defined in a simulation scenario, in which the mesh nodes on Cu and SiO_2 surfaces are not allowed to penetrate into each other. To calculate the average contact pressure (P) under a specific contact force (F), the local contact pressure values obtained at all individual nodes on the contact area are extracted and averaged.

FEA for Calculating the Magnitude of Electric Field. FEA (COMSOL Multiphysics software) is utilized to compute the electric field distribution associated with a rubbing-induced triboelectric charge pattern. In the computation, the surface charge density within the rubbed area is set to a specific value to let the resulted surface potential at the central line of the rubbed area equal to 100 mV, which is consistent with the corresponding potential value measured from our KPFM experiment. A set of charge conservation equations: $\mathbf{E} = -\nabla V$, $\nabla \cdot (\varepsilon_0 \varepsilon_r E) = \rho_v$ are subsequently solved to calculate the triboelectric field distribution.

Fabrication and Characterization of FETs and Memristors Based on RISS-Produced MoS_2 Lines. To fabricate back-gate FETs and memristors on RISS-produced MoS_2 line, interdigitated metallic drain/source contacts (5 nm Ti/50 nm Au) are fabricated by using photolithography followed with metallization. Specifically, 12 interdigitated contact pads are fabricated on each MoS_2 line. Therefore, there are 11 FETs or memristors fabricated on each RISS-produced MoS_2 line. The transport characteristics of FETs and memristors are measured using a Keithley 4200 semiconductor parameter analyzer. All the characteristic curves measured from working FETs and memristors are plotted in Figures S13 and S16, respectively.

DOI: 10.1021/acsami.8b15108
ACS Appl. Mater. Interfaces 2018, 10, 43774−43784

■ ASSOCIATED CONTENT

Supporting Information

The Supporting Information is available free of charge on the ACS Publications website at DOI: 10.1021/acsami.8b15108.

Triboelectric series of materials (Figure S1); rms roughness (R_q) values measured at rubbed and un-rubbed areas of the SiO_2 surface after rubbing process (Figure S2); XPS and water contact angle characterizations of a SiO_2 surface rubbed by a Cu rod template (Figure S3); surface potential under the heating (Figure S4); FEA contact configuration and mesh structures of Cu wire and SiO_2 surface (Figure S5); SEM and phase mode AFM images for investigating MoS_2 grain sizes (Figure S6); average thickness of RISS-produced MoS_2 lines (Figure S7); Raman characterization of RISS-produced MoS_2 (Figure S8); wide range Raman spectra obtained from RISS-produced MoS_2 line structures (Figure S9); comparison of electric field distribution obtained from KPFM and FEA (Figure S10); image processing process of a SEM image for extracting the cover ratio (Figure S11); SEM image Raman spectrum of 1 μm channel width MoS_2 FET (Figure S12); linear and semi-logarithmic I_{ds}–V_g curves obtained from 184 FETs (Figure S13); wide channel width FETs fabricated on RISS-produced MoS_2 line (Figure S14); TLM analysis of 1 μm channel width MoS_2 FET (Figure S15); pulse-programmed switching characteristic curves obtained from 10 memristors (Figure S16); and pulse-programmed switching characteristic curves obtained from a memristor transferred to a pristine SiO_2 substrate (Figure S17) (PDF)

A supplementary video showing a rubbing process driven by a lab-made rubbing tool (RISS Process.avi) (AVI)

■ AUTHOR INFORMATION

Corresponding Author

*E-mail: xiaoganl@umich.edu.

ORCID

Wei Lu: 0000-0002-4851-1032

Xiaogan Liang: 0000-0002-7390-9130

Author Contributions

The manuscript was written through contributions of all listed authors. All authors have given approval to the final version of the manuscript.

Notes

The authors declare no competing financial interest.

■ ACKNOWLEDGMENTS

This work is supported by the NSF grants # CMMI-1636132 and # ECCS-1708706. The authors would like to thank staffs of the University of Michigan's Lurie Nanofabrication Facility for providing the support of AFM/KPFM imaging and device fabrication, as well as Prof. Wei D. Lu's help with the access to the characterization tools for memristors.

■ ABBREVIATIONS

RISS method, rubbing-induced site-selective method
MoS_2, molybdenum disulfide
TMDC, transition metal dichalcogenide
SEM, scanning electron microscope
AFM, atomic force microscope
KPFM, kelvin probe microscope
FET, field-effect transistor

■ REFERENCES

(1) Li, H.; Tsai, C.; Koh, A. L.; Cai, L.; Contryman, A. W.; Fragapane, A. H.; Zhao, J.; Han, H. S.; Manoharan, H. C.; Abild-Pedersen, F.; Nørskov, J. K.; Zheng, X. Activating and optimizing MoS_2 basal planes for hydrogen evolution through the formation of strained sulphur vacancies. *Nat. Mater.* **2015**, *15*, 48−53.

(2) Lopez-Sanchez, O.; Lembke, D.; Kayci, M.; Radenovic, A.; Kis, A. Ultrasensitive Photodetectors Based on Monolayer MoS_2. *Nat. Nanotechnol.* **2013**, *8*, 497−501.

(3) Park, Y.; Ryu, B.; Oh, B.-R.; Song, Y.; Liang, X.; Kurabayashi, K. Biotunable Nanoplasmonic Filter on Few-Layer MoS_2 for Rapid and Highly Sensitive Cytokine Optoelectronic Immunosensing. *ACS Nano* **2017**, *11*, 5697−5705.

(4) Ryu, B.; Nam, H.; Oh, B.-R.; Song, Y.; Chen, P.; Park, Y.; Wan, W.; Kurabayashi, K.; Liang, X. Cyclewise Operation of Printed MoS_2 Transistor Biosensors for Rapid Biomolecule Quantification at Femtomolar Levels. *ACS Sens.* **2017**, *2*, 274−281.

(5) Ryu, B.; Yang, E.; Park, Y.; Kurabayashi, K.; Liang, X. Fabrication of Prebent MoS_2 Biosensors on Flexible Substrates. *J. Vac. Sci. Technol., B* **2017**, *35*, 06G805.

(6) Wi, S.; Kim, H.; Chen, M.; Nam, H.; Guo, L. J.; Meyhofer, E.; Liang, X. Enhancement of Photovoltaic Response in Multilayer MoS_2 Induced by Plasma Doping. *ACS Nano* **2014**, *8*, 5270−5281.

(7) Jang, Y.; Yeo, S.; Lee, H.-B.-R.; Kim, H.; Kim, S.-H. Wafer-scale, conformal and direct growth of MoS_2 thin films by atomic layer deposition. *Appl. Surf. Sci.* **2016**, *365*, 160−165.

(8) Desai, S. B.; Madhvapathy, S. R.; Amani, M.; Kiriya, D.; Hettick, M.; Tosun, M.; Zhou, Y.; Dubey, M.; Ager, J. W.; Chrzan, D.; Javey, A. Gold-Mediated Exfoliation of Ultralarge Optoelectronically-Perfect Monolayers. *Adv. Mater.* **2016**, *28*, 4053−4058.

(9) Li, D.; Wi, S.; Chen, M.; Ryu, B.; Liang, X. Nanoimprint-Assisted Shear Exfoliation Plus Transfer Printing for Producing Transition Metal Dichalcogenide Heterostructures. *J. Vac. Sci. Technol., B* **2016**, *34*, 06KA01.

(10) Nandi, D. K.; Sen, U. K.; Choudhury, D.; Mitra, S.; Sarkar, S. K. Atomic Layer Deposited MoS_2 As A Carbon and Binder Free Anode in Li-Ion Battery. *Electrochim. Acta* **2014**, *146*, 706−713.

(11) Robertson, J.; Liu, X.; Yue, C.; Escarra, M.; Wei, J. Wafer-Scale Synthesis of Monolayer and Few-Layer MoS_2 via Thermal Vapor Sulfurization. *2D Mater.* **2017**, *4*, 045007.

(12) Tan, L. K.; Liu, B.; Teng, J. H.; Guo, S.; Low, H. Y.; Loh, K. P. Atomic Layer Deposition of A MoS_2 Film. *Nanoscale* **2014**, *6*, 10584−10588.

(13) Yu, H.; Liao, M.; Zhao, W.; Liu, G.; Zhou, X. J.; Wei, Z.; Xu, X.; Liu, K.; Hu, Z.; Deng, K.; Zhou, S.; Shi, J.-A.; Gu, L.; Shen, C.; Zhang, T.; Du, L.; Xie, L.; Zhu, J.; Chen, W.; Yang, R.; Shi, D.; Zhang, G. Wafer-Scale Growth and Transfer of Highly-Oriented Monolayer MoS_2 Continuous Films. *ACS Nano* **2017**, *11*, 12001−12007.

(14) Addou, R.; McDonnell, S.; Barrera, D.; Guo, Z.; Azcatl, A.; Wang, J.; Zhu, H.; Hinkle, C. L.; Quevedo-Lopez, M.; Alshareef, H. N.; Colombo, L.; Hsu, J. W. P.; Wallace, R. M. Impurities and Electronic Property Variations of Natural MoS_2 Crystal Surfaces. *ACS Nano* **2015**, *9*, 9124−9133.

(15) Amani, M.; Chin, M. L.; Mazzoni, A. L.; Burke, R. A.; Najmaei, S.; Ajayan, P. M.; Lou, J.; Dubey, M. Growth-Substrate Induced Performance Degradation in Chemically Synthesized Monolayer MoS_2 Field Effect Transistors. *Appl. Phys. Lett.* **2014**, *104*, 203506.

(16) Ionescu, R.; George, A.; Ruiz, I.; Favors, Z.; Mutlu, Z.; Liu, C.; Ahmed, K.; Wu, R.; Jeong, J. S.; Zavala, L.; Mkhoyan, K. A.; Ozkan, M.; Ozkan, C. S. Oxygen etching of thick MoS_2 films. *Chem. Commun.* **2014**, *50*, 11226−11229.

(17) Jadwiszczak, J.; O'Callaghan, C.; Zhou, Y.; Fox, D. S.; Weitz, E.; Keane, D.; Cullen, C. P.; O'Reilly, I.; Downing, C.; Shmeliov, A.; Maguire, P.; Gough, J. J.; McGuinness, C.; Ferreira, M. S.; Bradley, A. L.; Boland, J. J.; Duesberg, G. S.; Nicolosi, V.; Zhang, H. Oxide-mediated recovery of field-effect mobility in plasma-treated MoS_2. *Sci. Adv.* **2018**, *4*, No. eaao5031.

DOI: 10.1021/acsami.8b15108
ACS Appl. Mater. Interfaces 2018, 10, 43774−43784

(18) Yang, S. Y.; Oh, J. G.; Jung, D. Y.; Choi, H.; Yu, C. H.; Shin, J.; Choi, C.-G.; Cho, B. J.; Choi, S.-Y. Metal-Etching-Free Direct Delamination and Transfer of Single-Layer Graphene with A High Degree of Freedom. *Small* **2014**, *11*, 175−181.
(19) Liu, Y.; Nan, H.; Wu, X.; Pan, W.; Wang, W.; Bai, J.; Zhao, W.; Sun, L.; Wang, X.; Ni, Z. Layer-by-Layer Thinning of MoS_2 by Plasma. *ACS Nano* **2013**, *7*, 4202−4209.
(20) Zhao, J.; Yu, H.; Chen, W.; Yang, R.; Zhu, J.; Liao, M.; Shi, D.; Zhang, G. Patterned Peeling 2D MoS_2 Off The Substrate. *ACS Appl. Mater. Interfaces* **2016**, *8*, 16546−16550.
(21) Han, G. H.; Kybert, N. J.; Naylor, C. H.; Lee, B. S.; Ping, J.; Park, J. H.; Kang, J.; Lee, S. Y.; Lee, Y. H.; Agarwal, R.; Johnson, A. T. C. Seeded Growth of Highly Crystalline Molybdenum Disulphide Monolayers at Controlled Locations. *Nat. Commun.* **2015**, *6*, 6128.
(22) Sun, D.; Nguyen, A. E.; Barroso, D.; Zhang, X.; Preciado, E.; Bobek, S.; Klee, V.; Mann, J.; Bartels, L. Chemical Vapor Deposition Growth of A Periodic Array of Single-Layer MoS_2 Islands via Lithographic Patterning of An SiO_2/Si Substrate. *2D Mater.* **2015**, *2*, 045014.
(23) Chen, X.; Park, Y. J.; Das, T.; Jang, H.; Lee, J.-B.; Ahn, J.-H. Lithography-Free Plasma-Induced Patterned Growth of MoS_2 and Its Heterojunction with Graphene. *Nanoscale* **2016**, *8*, 15181−15188.
(24) Zhou, Y. S.; Liu, Y.; Zhu, G.; Lin, Z.-H.; Pan, C.; Jing, Q.; Wang, Z. L. In Situ Quantitative Study of Nanoscale Triboelectrification and Patterning. *Nano Lett.* **2013**, *13*, 2771−2776.
(25) Hinchet, R.; Ghaffarinejad, A.; Lu, Y.; Hasani, J. Y.; Kim, S.-W.; Basset, P. Understanding and Modeling of Triboelectric-Electret Nanogenerator. *Nano Energy* **2018**, *47*, 401−409.
(26) Seol, M.-L.; Lee, S.-H.; Han, J.-W.; Kim, D.; Cho, G.-H.; Choi, Y.-K. Impact of Contact Pressure on Output Voltage of Triboelectric Nanogenerator Based on Deformation of Interfacial Structures. *Nano Energy* **2015**, *17*, 63−71.
(27) Kim, I. S.; Sangwan, V. K.; Jariwala, D.; Wood, J. D.; Park, S.; Chen, K.-S.; Shi, F.; Ruiz-Zepeda, F.; Ponce, A.; Jose-Yacaman, M.; Dravid, V. P.; Marks, T. J.; Hersam, M. C.; Lauhon, L. J. Influence of Stoichiometry on the Optical and Electrical Properties of Chemical Vapor Deposition Derived MoS_2. *ACS Nano* **2014**, *8*, 10551−10558.
(28) O'brien, M.; McEvoy, N.; Hallam, T.; Kim, H.-Y.; Berner, N. C.; Hanlon, D.; Lee, K.; Coleman, J. N.; Duesberg, G. S. Transition Metal Dichalcogenide Growth via Close Proximity Precursor Supply. *Sci. Rep.* **2014**, *4*, 7374.
(29) Homan, S. B.; Sangwan, V. K.; Balla, I.; Bergeron, H.; Weiss, E. A.; Hersam, M. C. Ultrafast Exciton Dissociation and Long-Lived Charge Separation in A Photovoltaic Pentacene−MoS_2 Van der Waals Heterojunction. *Nano Lett.* **2016**, *17*, 164−169.
(30) Zhang, Y.; Zhang, Y.; Ji, Q.; Ju, J.; Yuan, H.; Shi, J.; Gao, T.; Ma, D.; Liu, M.; Chen, Y.; Song, X.; Hwang, H. Y.; Cui, Y.; Liu, Z. Controlled Growth of High-Quality Monolayer WS_2 Layers on Sapphire and Imaging Its Grain Boundary. *ACS Nano* **2013**, *7*, 8963−8971.
(31) Kim, H.-J.; Kim, H.; Yang, S.; Kwon, J.-Y. Grains in Selectively Grown MoS_2 Thin Films. *Small* **2017**, *13*, 1702256.
(32) Li, H.; Zhang, Q.; Yap, C. C. R.; Tay, B. K.; Edwin, T. H. T.; Olivier, A.; Baillargeat, D. From Bulk to Monolayer MoS_2: Evolution of Raman Scattering. *Adv. Funct. Mater.* **2012**, *22*, 1385−1390.
(33) Boukhicha, M.; Calandra, M.; Measson, M.-A.; Lancry, O.; Shukla, A. Anharmonic Phonons in Few-Layer MoS_2: Raman Spectroscopy of Ultralow Energy Compression and Shear Modes. *Phys. Rev. B: Condens. Matter Mater. Phys.* **2013**, *87*, 195316.
(34) Hussain, S.; Shehzad, M. A.; Vikraman, D.; Khan, M. F.; Singh, J.; Choi, D.-C.; Seo, Y.; Eom, J.; Lee, W.-G.; Jung, J. Synthesis and Characterization of Large-Area and Continuous MoS_2 Atomic Layers by RF Magnetron Sputtering. *Nanoscale* **2016**, *8*, 4340−4347.
(35) Cheng, R.; Jiang, S.; Chen, Y.; Liu, Y.; Weiss, N.; Cheng, H.-C.; Wu, H.; Huang, Y.; Duan, X. Few-Layer Molybdenum Disulfide Transistors and Circuits for High-Speed Flexible Electronics. *Nat. Commun.* **2014**, *5*, 5143.
(36) Najmaei, S.; Liu, Z.; Zhou, W.; Zou, X.; Shi, G.; Lei, S.; Yakobson, B. I.; Idrobo, J.-C.; Ajayan, P. M.; Lou, J. Vapour Phase Growth and Grain Boundary Structure of Molybdenum Disulphide Atomic Layers. *Nat. Mater.* **2013**, *12*, 754−759.
(37) Otsu, N. A Threshold Selection Method from Gray-Level Histograms. *IEEE Trans. Syst. Man Cybern.* **1979**, *9*, 62−66.
(38) Zhou, C.; Wang, X.; Raju, S.; Lin, Z.; Villaroman, D.; Huang, B.; Chan, H. L.-W.; Chan, M.; Chai, Y. Low Voltage and High ON/OFF Ratio Field-Effect Transistors Based on CVD MoS_2 and Ultra High-k Gate Dielectric PZT. *Nanoscale* **2015**, *7*, 8695−8700.
(39) Ahn, J.-H.; Parkin, W. M.; Naylor, C. H.; Johnson, A. T. C.; Drndić, M. Ambient Effects on Electrical Characteristics of CVD-Grown Monolayer MoS_2 Field-Effect Transistors. *Sci. Rep.* **2017**, *7*, 4075.
(40) Bergeron, H.; Sangwan, V. K.; McMorrow, J. J.; Campbell, G. P.; Balla, I.; Liu, X.; Bedzyk, M. J.; Marks, T. J.; Hersam, M. C. Monolayer Chemical vapor deposition of monolayer MoS_2 directly on ultrathin Al2O3 for low-power electronics. *Appl. Phys. Lett.* **2017**, *110*, 053101.
(41) Subramanian, S.; Deng, D. D.; Xu, K.; Simonson, N.; Wang, K.; Zhang, K.; Li, J.; Feenstra, R.; Fullerton-Shirey, S. K.; Robinson, J. A. Properties of Synthetic Epitaxial Graphene/Molybdenum Disulfide Lateral Heterostructures. *Carbon* **2017**, *125*, 551−556.
(42) Sangwan, V. K.; Jariwala, D.; Kim, I. S.; Chen, K.-S.; Marks, T. J.; Lauhon, L. J.; Hersam, M. C. Gate-Tunable Memristive Phenomena Mediated by Grain Boundaries in Single-Layer MoS_2. *Nat. Nanotechnol.* **2015**, *10*, 403−406.
(43) Sangwan, V. K.; Lee, H.-S.; Bergeron, H.; Balla, I.; Beck, M. E.; Chen, K.-S.; Hersam, M. C. Multi-Terminal Memtransistors from Polycrystalline Monolayer Molybdenum Disulfide. *Nature* **2018**, *554*, 500−504.
(44) Li, C.; Hu, M.; Li, Y.; Jiang, H.; Ge, N.; Montgomery, E.; Zhang, J.; Song, W.; Dávila, N.; Graves, C. E.; Li, Z.; Strachan, J. P.; Lin, P.; Wang, Z.; Barnell, M.; Wu, Q.; Williams, R. S.; Yang, J. J.; Xia, Q. Analogue Signal and Image Processing with Large Memristor Crossbars. *Nat. Electron.* **2017**, *1*, 52−59.

DOI: 10.1021/acsami.8b15108
ACS Appl. Mater. Interfaces 2018, 10, 43774−43784